UC San Diego
Oceanography Program Publications

Title
Tsunami and infragravity waves impacting Antarctic ice shelves

Permalink
https://escholarship.org/uc/item/3f89k693

Journal
Journal of Geophysical Research: Oceans, 122(7)

ISSN
2169-9275 2169-9291

Authors
Bromirski, P. D
Chen, Z.
Stephen, R. A
et al.

Publication Date
2017-07-20

DOI
10.1002/2017JC012913

Data Availability
The data associated with this publication are available upon request.

Peer reviewed

eScholarship.org Powered by the California Digital Library
University of California

AGU PUBLICATIONS

JGR

Journal of Geophysical Research: Oceans

RESEARCH ARTICLE

10.1002/2017JC012913

Tsunami and infragravity waves impacting Antarctic ice shelves

P. D. Bromirski[1], Z. Chen[1], R. A. Stephen[2], P. Gerstoft[1], D. Arcas[3], A. Diez[4], R. C. Aster[5], D. A. Wiens[6], and A. Nyblade[7]

[1]Scripps Institution of Oceanography, University of California San Diego, La Jolla, California, USA, [2] Department of Geology and Geophysics, Woods Hole Oceanographic Institution, Woods Hole, Massachusetts, USA, [3]National Oceanic and Atmospheric Administration-Pacific Marine Environmental Laboratory, Joint Institute for the Study of the Atmosphere and Ocean, University of Washington, Seattle, Washington, USA, [4]Science Research Department, Norwegian Polar Institute, Tromsø, Norway, [5]Department of Geosciences and Warner College of Natural Resources, Colorado State University, Fort Collins, Colorado, USA, [6]Department of Earth and Planetary Sciences, Washington University in St. Louis, St. Louis, Missouri, USA, [7]Department of Geosciences, Penn State University, University Park, Pennsylvania, USA

Key Points:
- The first broadband seismometer recordings of ice shelf tsunami impacts indicate that flexural-gravity waves are the dominate response
- Very long period (>300 s) flexural-gravity waves are excited year-round, with the horizontal displacements >20 cm largest during the austral winter
- Bathymetry under and north of the RIS focuses gravity wave energy to particular locations along the front where tabular iceberg has occurred

Supporting Information:
- Supporting Information S1
- Movie S1
- Movie S2

Correspondence to:
P. D. Bromirski,
pbromirski@ucsd.edu

Citation:
Bromirski, P. D., Z. Chen, R. A. Stephen, P. Gerstoft, D. Arcas, A. Diez, R. C. Aster, D. A. Wiens, and A. Nyblade (2017), Tsunami and infragravity waves impacting Antarctic ice shelves, *J. Geophys. Res. Oceans*, *122*, doi:10.1002/2017JC012913.

Received 29 MAR 2017
Accepted 13 JUN 2017
Accepted article online 16 JUN 2017

Abstract The responses of the Ross Ice Shelf (RIS) to the 16 September 2015 8.3 (M_w) Chilean earthquake tsunami (>75 s period) and to oceanic infragravity (IG) waves (50–300 s period) were recorded by a broadband seismic array deployed on the RIS from November 2014 to November 2016. Here we show that tsunami and IG-generated signals within the RIS propagate at gravity wave speeds (~70 m/s) as water-ice coupled flexural-gravity waves. IG band signals show measureable attenuation away from the shelf front. The response of the RIS to Chilean tsunami arrivals is compared with modeled tsunami forcing to assess ice shelf flexural-gravity wave excitation by very long period (VLP; >300 s) gravity waves. Displacements across the RIS are affected by gravity wave incident direction, bathymetry under and north of the shelf, and water layer and ice shelf thicknesses. Horizontal displacements are typically about 10 times larger than vertical displacements, producing dynamical extensional motions that may facilitate expansion of existing fractures. VLP excitation is continuously observed throughout the year, with horizontal displacements highest during the austral winter with amplitudes exceeding 20 cm. Because VLP flexural-gravity waves exhibit no discernable attenuation, this energy must propagate to the grounding zone. Both IG and VLP band flexural-gravity waves excite mechanical perturbations of the RIS that likely promote tabular iceberg calving, consequently affecting ice shelf evolution. Understanding these ocean-excited mechanical interactions is important to determine their effect on ice shelf stability to reduce uncertainty in the magnitude and rate of global sea level rise.

Plain Language Summary A major source of the uncertainty in the magnitude and rate of global sea level rise is the contribution from Antarctica. Ice shelves buttress land ice, restraining land ice from reaching the sea. We present the analysis of seismic data collected with a broadband seismic array deployed on the Ross Ice Shelf, Antarctica. The characteristics of ocean gravity-wave-induced vibrations, that may expand existing fractures in the ice shelf and/or trigger iceberg calving or ice shelf collapse events, are described. The mechanical dynamic strains induced can potentially affect ice shelf integrity, and ultimately reduce or remove buttressing restraints, accelerating sea level rise.

1. Introduction

The integrity and evolution of buttressing Antarctic ice shelves are key factors that contribute to the uncertainty in predicting the rate of sea level rise over the coming decades [*Dupont and Alley*, 2005; *Bromwich and Nicolas*, 2010; *Gudmundsson*, 2013]. The acceleration of outlet glaciers after the breakup of the Larsen B Ice Shelf [*Rignot et al.*, 2004; *Scambos et al.*, 2004] underscores the importance of ice shelves to restrain grounded ice from reaching the ocean. The collapse and disintegration of Antarctic Peninsula ice shelves over the past three decades has been attributed to hydrofracturing [*Scambos et al.*, 2009; *Banwell et al.*, 2013] and buoyancy-induced bending stresses [*Braun et al.*, 2009; *Scambos et al.*, 2009], with ice shelf thinning from basal melting contributing to weakening and fracturing. These factors will be exacerbated by rising ocean and atmosphere temperatures, which will have a negative impact on ice shelf stability [*Joughin and Alley*, 2011].

© 2017. American Geophysical Union. All Rights Reserved.

Because of the importance of surface melt ponds in hydrofracturing [*MacAyeal et al*., 2015], major ice shelf calving/collapse sequences typically occur during the latter part of the austral summer (e.g., Larsen B in February 2002, *Rack and Rott* [2004] and Wilkins in February 2008, *Braun et al*. [2009]). However, satellite imagery indicates that ice shelf disintegration events have also occurred during the austral fall (Wilkins in April 2009) when free surface water (ponding) was likely minimal. Other examples of austral fall/winter fracture events include the calving of tabular icebergs at the more southern Ross Ice Shelf where free surface water does not occur, for example, B-15 in March 2000. Furthermore, recent satellite imagery shows episodic ongoing extension of a major rift system in the Larsen C ice shelf between March and August 2016 (http://www.projectmidas.org/blog/a-growing-rift-in-larsen-c/). What triggers specific ice shelf calving, rifting, or collapse events in either the austral summer or winter is an open question, although a potential contributing process is ocean gravity wave forcing [*Holdsworth and Glynn*, 1978; *Bromirski et al*., 2010; *Brunt et al*., 2011; *Sergienko*, 2013]. Here we show that gravity wave forcing produces episodic displacements across the Ross Ice Shelf (RIS) that potentially can trigger or abet fracturing. A better understanding of the mechanical impacts of ocean gravity waves on ice shelves will improve modeling of ice shelf/ice sheet evolution to anticipate the rate of sea level rise.

The importance of flexural-gravity wave excitation on ice shelf evolution (e.g., in crack expansion and fracture triggering) depends on the distribution of induced displacements, stresses, and strains across the ice shelf. Vertical displacements will produce bending stresses [*Holdsworth and Glynn*, 1978; *Sergienko*, 2013], while horizontal displacements potentially induce extensional stresses that can facilitate crack expansion. Previous single-station ice shelf seismic measurements on the Ross Ice Shelf (RIS) show a strong RIS response to swell in the 10–30 s period band, particularly during the austral summer when sea ice is absent north of the RIS front [*MacAyeal et al*., 2006; *Cathles et al*., 2009]. Longer period gravity waves, infragravity waves (IG, $>$50 s period), generated by swell transformation along coasts [*Herbers et al*., 1995] and under storms in the deep ocean [*Uchiyama and McWilliams*, 2008], provide an additional forcing of ice shelves.

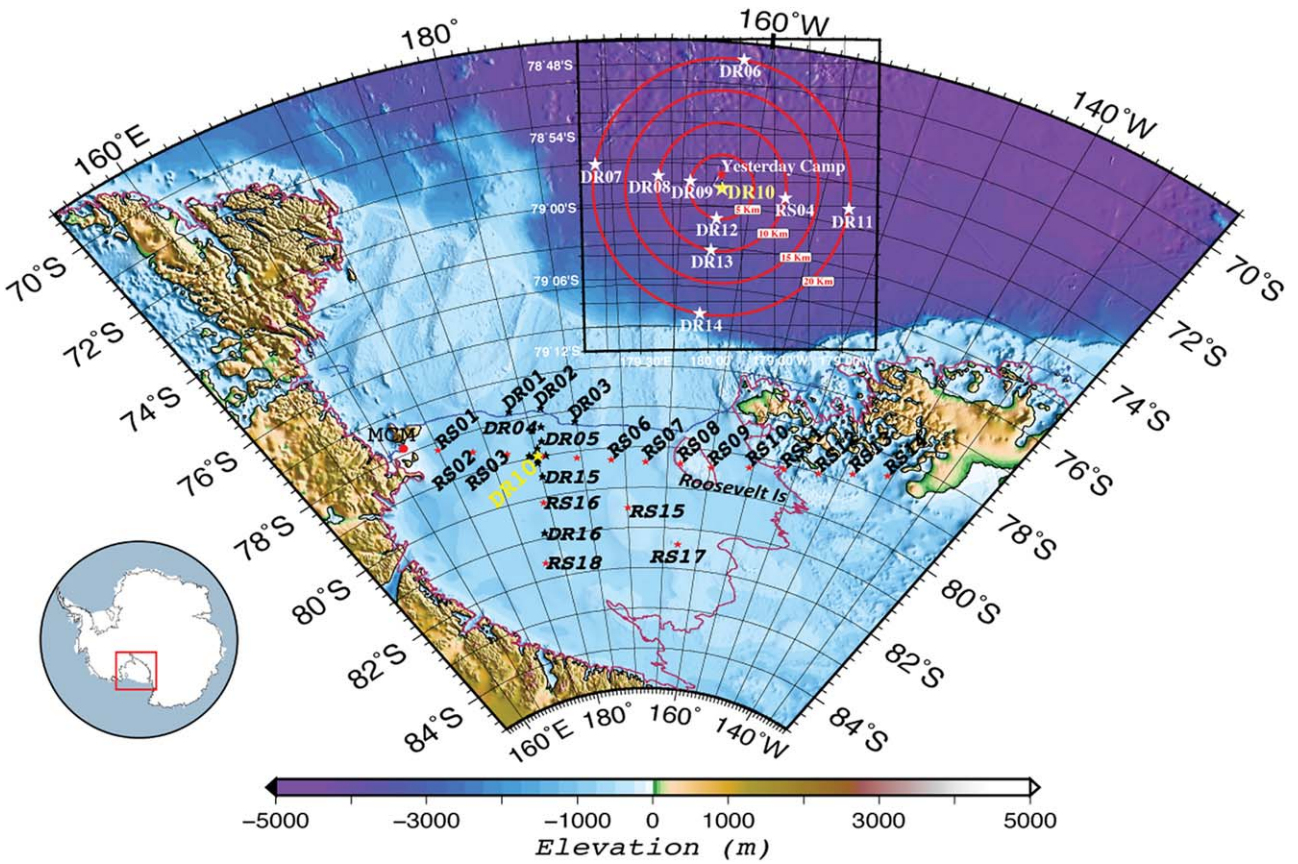

Figure 1. Locations of seismic stations (stars) on the Ross Ice Shelf (RIS) overlying bathymetry of the Ross Sea embayment. Front of the ice shelf (blue line) and grounding zone (magenta line) are indicated. (Insert) Station distribution of the high-density subarray centered at DR10 (yellow star), located near deep-field Yesterday Camp (red star), with 5 km rings from DR10 in red.

Importantly, IG waves generated along the Pacific coast of North America and by storm activity in the Southern Ocean [*Bromirski et al*., 2010; *Bromirski and Stephen*, 2012; *Bromirski et al*., 2015] excite a much higher RIS response than does swell.

To characterize the RIS response to IG wave and swell activity, a three-component 34-station broadband seismic array (Figure 1) was deployed from November 2014 to November 2016 [*Bromirski et al*., 2015]. Each seismic station was equipped with self-leveling three-component Nanometrics T120 PHQ seismometers and Quanterra Q330 digitizers. Preliminary results from 2 weeks of data collected in November 2014 from three stations (DR09, DR10, and DR13) suggested that IG waves generate water/ice coupled flexural-gravity waves that propagate southward from the shelf front [*Bromirski et al*., 2015; *Diez et al*., 2016]. However, three closely situated stations within 10 km of each other were insufficient to adequately describe the gravity wave-induced signal propagation characteristics or their spatial variability. Here we present analysis from the entire array over a full year to describe the dominant RIS responses to ocean forcing, and their potential impacts on RIS integrity. The RIS response to gravity wave excitation over November 2014 to November 2015 is enhanced by understanding the variability of seismic displacements across the RIS resulting from September 2015 Chilean tsunami [*Aránguiz et al*., 2016] impacts.

2. Spatial Variability of Chilean Tsunami and IG-Induced RIS Vibrations

Serendipitous recordings of the September 2015 Chilean tsunami by the RIS array enable investigation of the RIS response to very long period gravity wave excitation. Tsunamis in the far field have energy at frequencies $<$0.02 Hz, and so can contain energy in the IG band as well as at lower frequencies. The great circle path to the RIS from the associated earthquake rupture (31.570°S, 71.654°W) passes through Marie Byrd Land, blocking the direct tsunami from reaching the RIS. To reach the RIS, the tsunami must therefore undergo substantial scattering and refraction from seamounts and other bathymetric features [*Rasmussen et al*., 2015].

Variation in ocean-induced displacements across the RIS results from several factors: (1) changes in ice shelf thickness and elastic properties, (2) ice shelf structure local to the seismic stations, (3) bathymetry below the RIS, and (4) attenuation of IG wave-induced RIS excitation. A representative strong IG event during May 2015, with RIS amplitudes similar to the tsunami near the shelf front, was selected for comparison of IG-induced RIS responses with tsunami. The vertical displacements of the RIS under tsunami excitation show relatively little decrease in amplitude with distance south of the shelf front, from DR02 to DR16 (Figures 2a–2c). In contrast to tsunami excitation, displacements resulting from meteorologically-generated IG wave impacts recorded in May (Figures 2d–2f) show markedly greater attenuation. For this reason, the tsunami produced the highest amplitude gravity wave-generated RIS response recorded away from the ice edge, although IG-wave-forced events can have comparable energy at the shelf front (compare Figures 2a and 2d).

Changes in median power spectral density for the north-south station transect, roughly orthogonal to the RIS front (DR02–RS18; Figure 1), are used to characterize the spatial variation of the RIS response away from the front toward the grounding line to tsunami (Figures 3a and 3c) and other IG wave-induced (Figures 3b and 3d) signals. Inflection points in the spectra near 0.03 Hz in Figure 3 indicate the swell-to-IG wave transition frequency. To exclude the lowest frequency swell energy from IG band analyses, we choose the 0.003–0.02 Hz ($\sim$300–50 s period) frequency band to represent IG wave excitation (the pass-band employed in Figures 2d–2f). Spectral levels in the 0.001–0.003 Hz (1000–300 s period) band were chosen to characterize tsunami and other very long period (VLP) flexural-gravity wave variability.

Peak IG band vertical spectral levels during the May IG event are about 10 dB higher than during the tsunami. Furthermore, signal levels in the IG band for this event are about 10 dB higher than during a representative quiet period when minimal gravity wave excitation occurred (see supporting information Figure S7). Vertical and north-south (N-S) horizontal component spectral levels in the IG band decrease systematically with distance from the ice front for both tsunami and IG events, and exhibit an associated spectral peak shift to lower frequencies. This signal attenuation results from ice shelf damping of flexural-gravity wave energy in the IG band, causing the decrease in vertical displacement amplitudes with distance from the front (Figures 2d–2f), and resulting in only a small contribution of IG band energy to displacement levels at DR16 (Figure 2f). Vertical displacements in the VLP band (supporting information Figure S3, bandpass-filtered from 0.001 to 0.003 Hz) are comparable to Figures 2a–2c, with the relatively small differences in amplitudes with

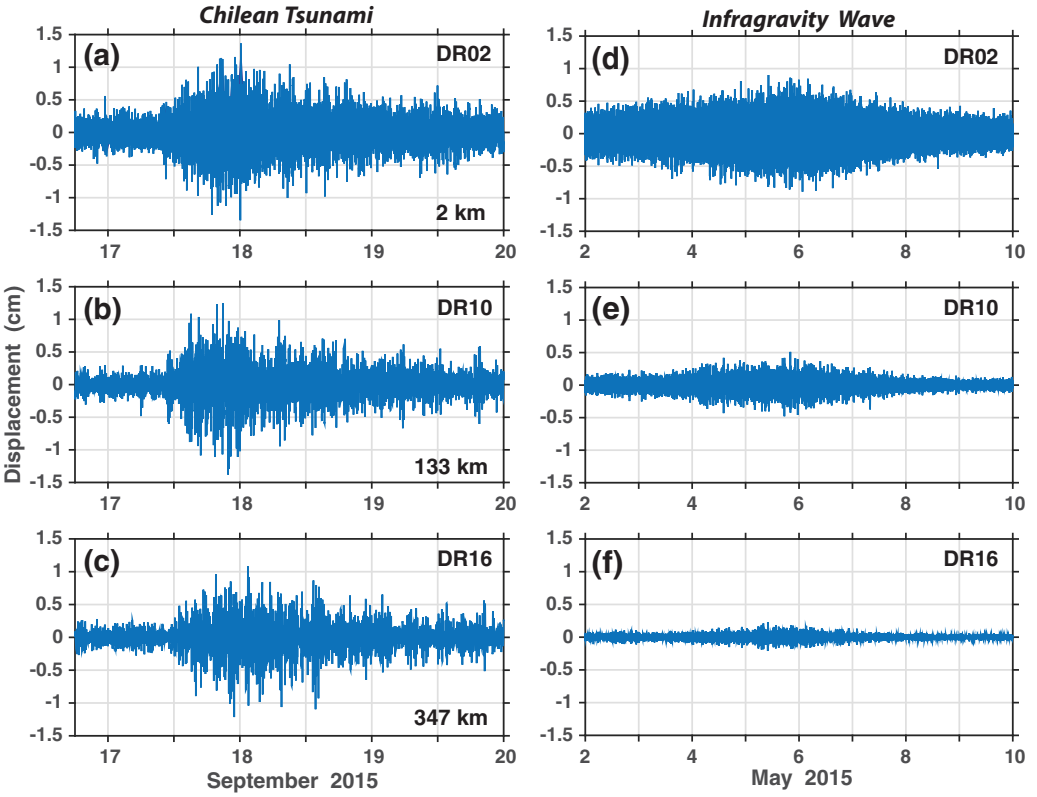

Figure 2. (a–c) Vertical displacement response of the RIS during the arrival of the Chilean September 2015 tsunami (band pass-filtered from 0.001 to 0.4 Hz) at stations progressively farther from RIS front (distance from front in km at lower right). (d–f) Vertical displacement amplitudes during a strong infragravity (IG) wave event that occurred in May 2015 (band pass-filtered from 0.003 to 0.02 Hz).

distance from the front resulting from attenuation of tsunami-contained IG band energy, and confirming that most of the tsunami energy is in the VLP band, i.e., at frequencies $<$0.003 Hz.

The systematic monotonic decrease in IG band energy from the shelf front toward the grounding line persists down to 0.003 Hz (about 300 s period), below which spectral levels show little variability across the RIS (Figure 3). Signal levels in the VLP band are about 10 dB higher than during the quiet period (supporting information Figure S7). At gravity wave periods $>$300 s, the gravity wave wavelengths (supporting information Figure S4b) are evidently too long compared with the ice thickness (about 300 m, *Bromirski et al.* [2015]) for the ice shelf to significantly affect flexural-gravity wave propagation [*Fox and Squire*, 1991; *Sergienko*, 2010]. Similarly, sea ice (2–5 m thick) has a minimal effect on IG wave and long period (25–30 s) swell propagation [*Wadhams and Doble*, 2009; *Squire*, 2007]. The small differences in spectral levels at frequencies $<$0.003 Hz (Figure 3), i.e., the lack of discernable attenuation with distance from the front in this band, indicates that the propagation of much longer wavelength VLP flexural-gravity waves across the RIS is not appreciably affected by the 200–400 m thick ice shelf. Thus, flexural-gravity wave energy in the VLP band readily propagates to the grounding zone.

3. Water-Ice-Coupled Flexural-Gravity Wave Propagation Characteristics From Beamforming

Ice shelf flexural-gravity wave theory can be derived from excitation of a "thin" floating plate where the ice shelf thickness is much less than the forcing wavelengths [*Fox and Squire*, 1991; *Sergienko*, 2010]. Long wavelength tsunami and IG wave energy excite flexural-gravity waves, i.e., coupled ice/water flexural-gravity waves that propagate near ocean gravity wave speeds. The amount of gravity wave energy within the subshelf cavity depends on the frequencies (and associated wavelengths) of the incident gravity waves. Only longer period, longer wavelength gravity waves, that have sufficient energy below the base of the ice shelf to enter the ice shelf cavity, can couple into flexural-gravity waves. Other ice shelf "plate waves"

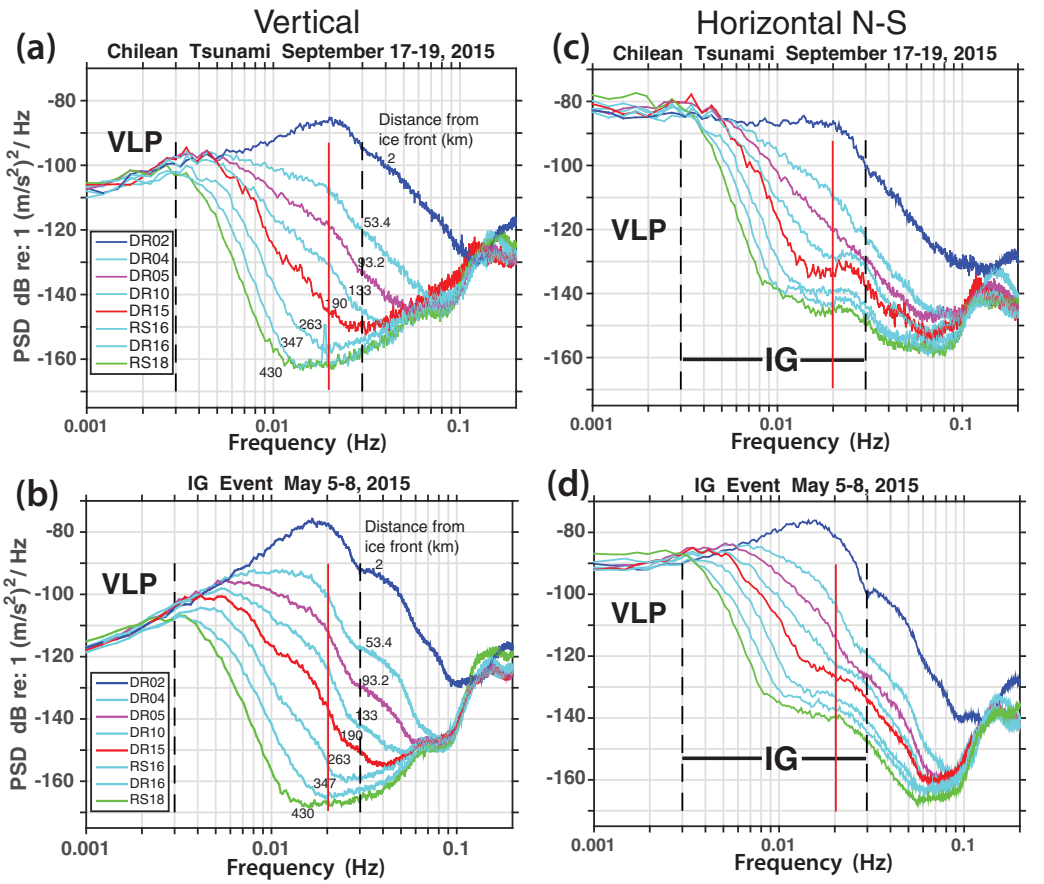

Figure 3. (a and c) Median acceleration response spectral levels of tsunami and (b and d) infragravity (IG) wave events at seismic stations along the transect roughly orthogonal to the RIS shelf front. Legends give station identifications ordered by distance from the ice edge (see Figure 1 for station locations). (a and b) Median spectra are shown for vertical and (N-S, c and d) north-south horizontal components over the time periods indicated in the plot titles. Vertical dashed lines indicate the IG and very long period (VLP, 0.001–0.003 Hz) band limits. To ensure that the lowest frequency swell energy does not contaminate IG wave analyses, the band is restricted to (0.003–0.02 Hz), with the IG analysis upper frequency bound indicated by the vertical red line. Spectra for the stations are ordered according to distance from the front (highest levels are at front station DR02), with levels in the IG band decreasing monotonically south of the front.

excited by ocean gravity wave interactions include flexural (asymmetric) and extensional (symmetric) Lamb waves [*Lamb*, 1917; *Press and Ewing*, 1951; *Graff*, 1975]. Flexural Lamb waves have dominant vertical motions, while extensional Lamb waves have dominant horizontal motions. Extensional Lamb waves propagate at higher phase velocities than either flexural-gravity waves or flexural Lamb waves, which facilitate their differentiation.

Frequency-domain beamforming [*Gerstoft and Tanimoto*, 2007] is used to extract propagation characteristics and source direction of coherent gravity wave-induced signals propagating across the RIS array. To reduce aliasing resulting from the array geometry, only the closely sited subarray (approximately 130 km from the ice front) stations near DR10 (within 20 km, Figure 1, insert), plus DR05, DR15, RS03, and RS05 in Figure 1; 14 stations total) were used in the beamforming. Before beamforming, each spectral estimate on each station component was energy-normalized to retain only its phase. Beamforming was performed for 4096 s data segments, with beamformer power stacked over the event time interval for azimuths (−45° to 45°) spanning a slowness range of 0–25 s/km, giving the dispersion characteristics of the signals.

A strong IG wave-induced event over 5–8 May 2015 was used to assess the RIS response in the absence of tsunami excitation. Beamforming of the tsunami and IG events yields the frequency-slowness (f-s) radial-component beam power energy dispersion distributions (Figures 4a and 4b). The peaks in beam power (black dots in Figures 4a and 4b) have dominant slownesses near 15 s/km, giving phase speeds comparable to shallow-water ocean surface gravity waves in this frequency band (phase speed = 1/slowness) of about 70 m/s. Tsunami-generated peak beam power occurs at a lower frequency than the peak IG response

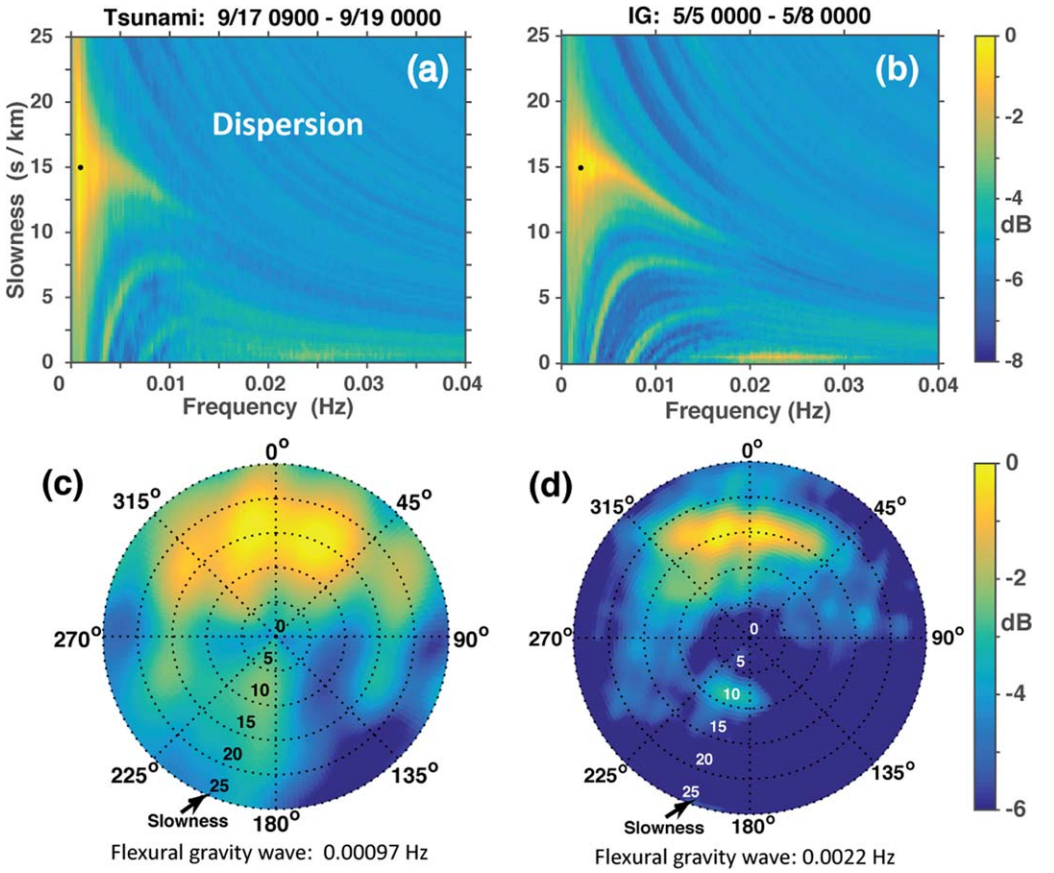

Figure 4. Tsunami and IG wave beamforming of seismic data from 14 stations clustered around DR10, approximately 130 km from the ice front (those shown in the Figure 1 insert), plus RS03, RS05, DR05, and DR15. Frequency-slowness (f-s) dispersion plots showing the *radial*-component beam power distribution (in dB) for (a) Tsunami (normalized to a maximum of 0 dB, normalization = 5.23 dB) and (b) Infragravity wave (IG; normalization = 5.64 dB) events during the time periods given in the panel titles. (c and d) Back azimuth beam power distributions at the f-s peak power (frequencies identified by black dots in Figures 4a and 4b, with respective peak-power frequencies indicated below the panels) for the tsunami and IG events, respectively. To emphasize the dominant beam power patterns, plots were normalized by the maximum power in respective panels. Hyperboloid bands in Figures 4a and 4b are processing artifacts resulting from aliasing due to the array configuration.

(Figure 3; black dots in Figures 4a and 4b). These results are consistent with flexural-gravity wave theory [*Fox and Squire*, 1991] and with prior IG wave-generated flexural-gravity wave measurements determined using a sparse gravimeter array on the RIS [*Williams and Robinson*, 1981].

The lack of significant beam power at frequencies above 0.02 Hz for slownesses near 15 s/km in Figures 4a and 4b indicates that gravity waves at these and higher frequencies generally produce relatively little flexing of the RIS, because either insufficient swell energy penetrates the subshelf cavity to generate coherent flexural-gravity wave energy across the array. This follows from the exponential gravity wave pressure decay with depth (supporting information Figure S4a), where higher frequency swell decays much more rapidly than lower frequency IG waves, resulting in proportionately more energy penetrating the cavity as frequency decreases and gravity wave wavelength increases (supporting information Figure S4b). Alternatively, the station spacing may be too large for higher frequency, shorter wavelength coherent signal detection.

Relatively high beam power in the 0.02–0.025 Hz band at low slowness in Figure 4b (this energy is below swell frequencies) indicates that some higher-frequency IG wave energy is converted into higher phase velocity extensional Lamb waves that propagate horizontally within the ice shelf. This energy has a slowness of about 0.35 s/km, corresponding to a phase velocity of about 2800 m/s, which is about 1.8 times the shear wave speed in ice [*Diez et al*., 2016]. Differences between Figures 4a and 4b at slowness <1 s/km reflect differences in incident gravity wave spectral energy distributions, with lower extensional Lamb-wave beam

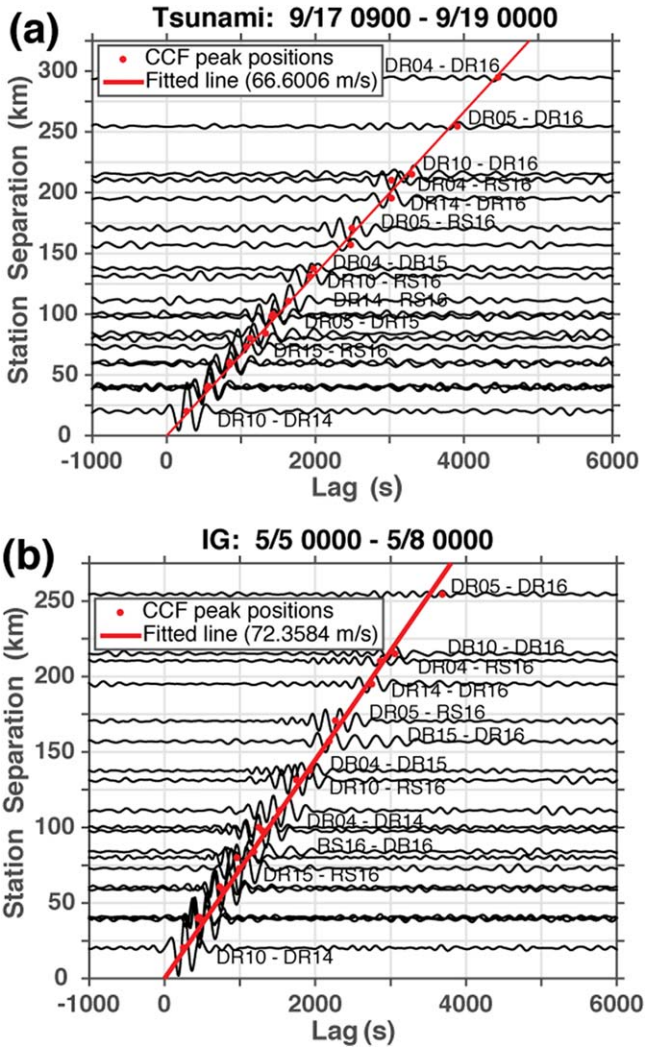

Figure 5. (a) Cross-correlation functions (CCF) between orthogonal transect station pairs DR04, DR05, DR10, DR14, DR15, RS16, and DR16 for the tsunami in the [0.001, 0.01] Hz band for the N-S horizontal component. Key station pairs are identified. (b) Same as (a) except for the IG event in the [0.003, 0.02] Hz band during 5–8 May 2015. CCF peaks (red dots) were determined from respective envelope functions of each CCF.

power in Figure 4a consistent with lower IG band energy impacting the RIS during the tsunami than during the strong IG event, which has spectral levels near 0.02 Hz that are about 5 dB higher (Figure 3).

As expected for ocean waves impacting the RIS, beamforming indicates that signals propagate from the north, i.e., where gravity waves initially impact the shelf front (Figures 4c and 4d). For the Chilean tsunami, the dominant azimuth is from the northeast at about 30°, with signals propagating from an additional significant source region at about 350°. These beam power source directions show that flexural-gravity waves are generated over much of the shelf front, with some IG-induced signals arriving from northeast quadrant directions that are approximately in common with the tsunami-generated signal propagation azimuths.

Cross correlations of radial-component waveforms [*Harmon et al.*, 2010] over the tsunami and May IG events were done to confirm beamforming phase velocity estimates across the array. The raw data were demeaned, filtered between 0.003 and 0.02 Hz for IG and 0.001 and 0.01 Hz for tsunami, and then cross correlated between station pairs in the time domain using OBSPY [*Beyreuther et al.*, 2010]. Only station pairs across the orthogonal transect (DR04, DR05, DR06, DR10, DR14, DR15, and RS16) with high cross-correlation function (CCF) values (Figure 5) used to estimate the phase velocities. Least squares fit to the time-domain CCF peaks gives phase speeds near 70 m/s for both tsunami and IG events (Figures 5a and 5b, respectively). These phase speeds agree closely with the slowness (15 s/km $\sim$ 70 m/s) obtained from beamforming (Figure 4), and are consistent with flexural-gravity wave propagation at shallow-water gravity wave speeds.

4. Seasonally Variable VLP Gravity Wave Forcing

These unprecedented year-round ice shelf broadband seismic observations afford the opportunity to investigate seasonal variability of the RIS response to gravity wave forcing, and hence by inference the variability of the ocean forcing. Because IG band flexural-gravity wave energy attenuates systematically southward from the front (Figures 2 and 3), we characterize the austral winter RIS response focusing on seismic station DR16, located about 350 km from the shelf front where signal levels are dominated by flexural-gravity wave energy in the VLP band. Year-round horizontal displacements are about 10–20 times greater than vertical displacements. Surprisingly, the highest displacements observed at DR16 occur during the austral winter (Figures 6a and 6b) when sea ice reaches a maximum and associated sea-ice gravity wave damping [e.g., *Bromirski and Stephen*, 2012; *Anthony*

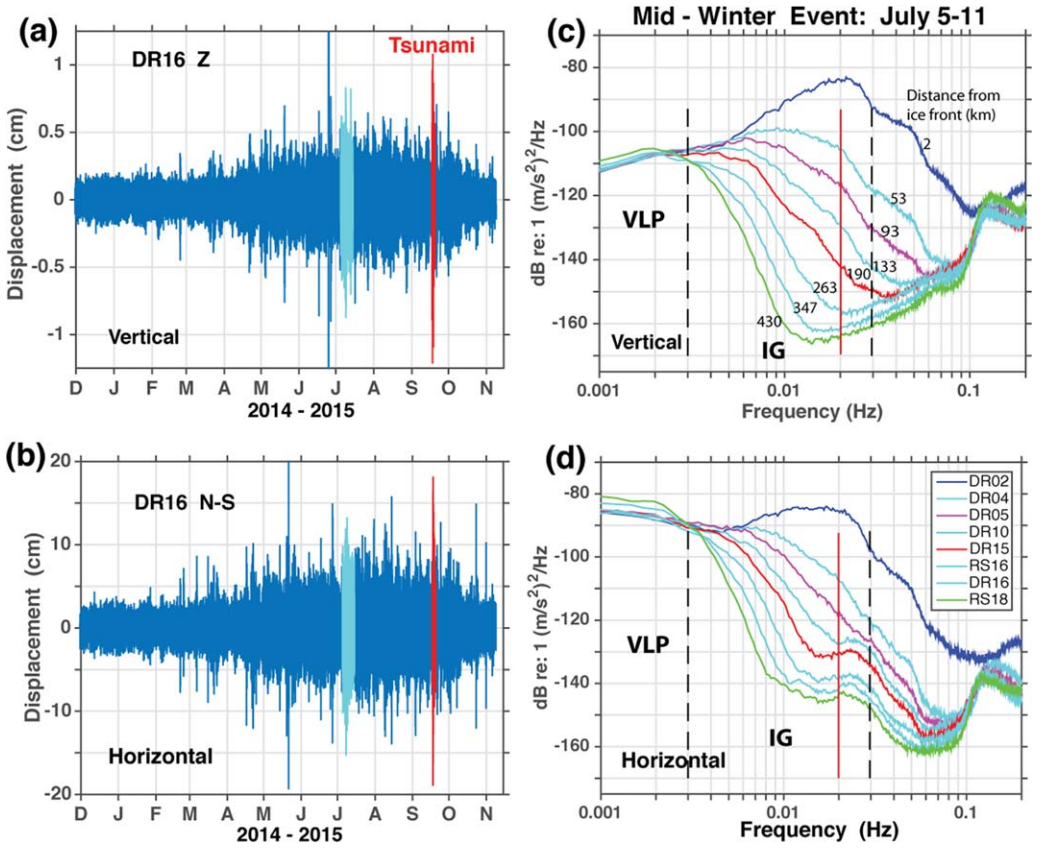

Figure 6. Seasonal (austral winter) variability. (a) Vertical (Z) displacement response (band pass-filtered from 0.001 to 0.4 Hz) at seismic station DR16, located about 350 km south of the ice edge. The Chilean tsunami event (red) and a particularly strong mid-winter 5–11 July event (cyan) are identified. (b) Same as (a) except showing the north-south (N-S) horizontal component response. Note that the displacement scales differ significantly. (c) Median vertical component spectral levels for the 5–11 July event shown in Figure 6a at the same orthogonal transect stations used in Figure 3. (d) Same as (c) except for the horizontal response shown in Figure 6b. Legend in Figure 6d applies to Figure 6c. Spectra for the stations are ordered according to distance from the front (highest levels are at front station DR02), with levels in the IG band decreasing monotonically south of the front.

et al., 2017] might be expected to reduce gravity wave generation in the Ross Sea region and subsequent forcing of the ice shelf. However, we find that typical vertical and horizontal RIS displacements in the VLP band are about a factor of 10 greater in the austral winter compared to the austral summer.

The mid-winter RIS response to VLP forcing is characterized by an event during 5–11 July 2015 (Figures 6a and 6b, highlighted in cyan). The vertical and horizontal displacements at DR16 for the July event are comparable to the tsunami (highlighted in red) and other events throughout June–October, indicating that VLP gravity waves commonly produce peak-to-trough horizontal RIS displacements higher than 20 cm during the austral winter, with vertical displacements commonly greater than 1 cm. At stations closer to the shelf front, austral winter spectral levels are comparable to those during the tsunami and the May 2015 IG events in both the VLP and IG bands (compare Figures 3 and 6c, 6d), indicating that similar gravity wave excitation of the RIS occurs throughout the year. Horizontal component spectral levels below 0.003 Hz during the July event (Figure 6d) are comparable to the tsunami (Figure 3c).

The presence of sea ice during the austral winter inhibits ocean gravity wave generation over the Ross Sea, suggesting that nongravity wave associated meteorological forcing directly over the RIS may excite the observed VLP RIS response [*Crocker and Wadhams*, 1988]. However, beamforming of the strong event during July 2015 (using the same station subset as in Figure 4) indicates that these signals propagate from the north at gravity wave speeds (∼70 m/s, 15 s/km), i.e., from the shelf front (Figure 7b). These propagation characteristics indicate that these are flexural-gravity waves resulting from ice-ocean interactions, and are not forced by atmospheric variability directly over the RIS. However, coupling of atmosphere pressure fluctuations through the sea ice north of the RIS may provide the forcing at the shelf front [*Crocker and*

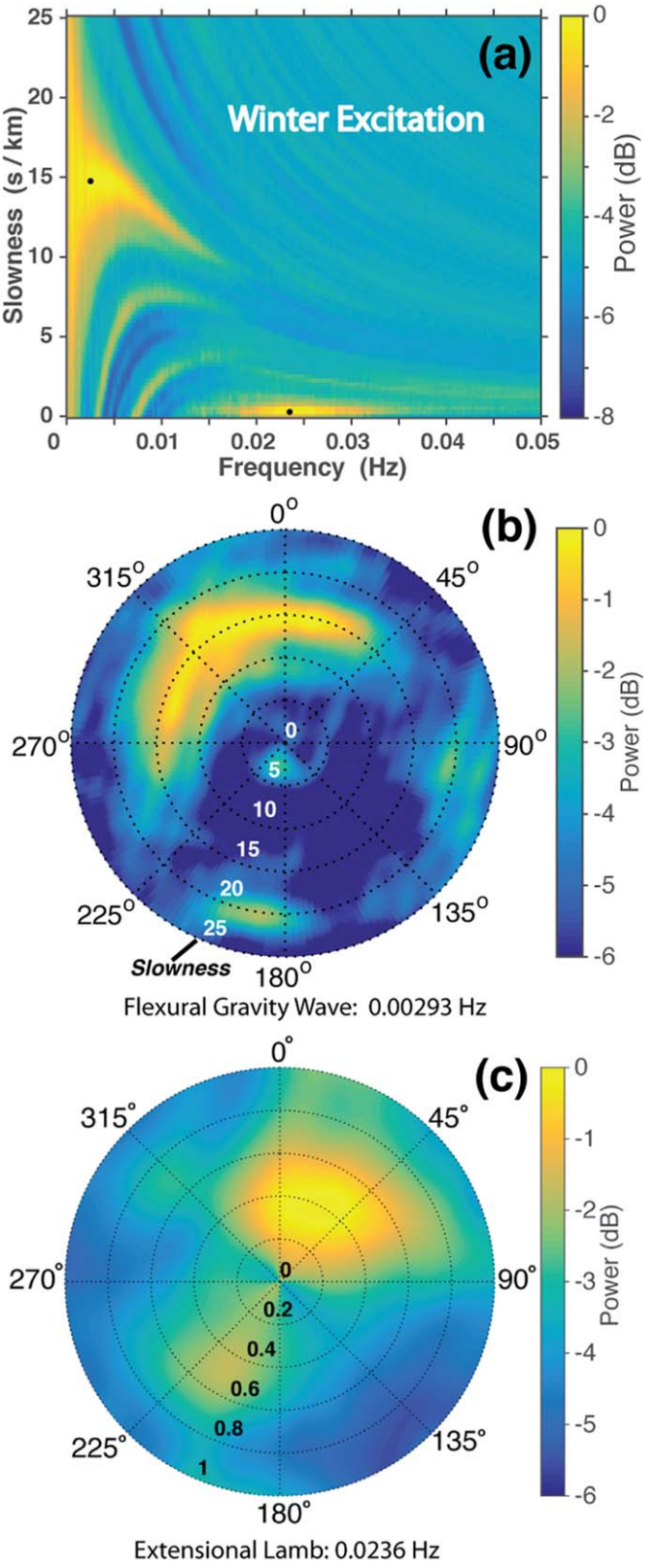

Figure 7. (a) Beam formed frequency-slowness (f-s) radial-component outputs for the mid-winter 5–11 July event (normalized to a maximum of 0 dB, normalization = 4.75 dB), with black dots identifying the peak power for the high slowness (~15 s/km (~70 m/s phase velocity) flexural-gravity wave) and low slowness (~0.35 s/km (~2.8 km/s) extensional Lamb wave) phases. Peak power frequencies (black dots) that identify respective beam power snapshots are shown below (b) and (c). (b) Propagation back azimuths of the high slowness flexural-gravity waves. (c) Propagation back azimuths of the low slowness IG/swell band extensional Lamb wave signals.

Wadhams, 1988]. The occurrence of heightened VLP band RIS responses during the austral winter strongly suggests an association with storm activity in the Southern Ocean.

It is unclear whether VLP waves are generated under storms in the deep-ocean [*Uchiyama and McWilliams*, 2008; *Traer and Gerstoft*, 2014], result from near-coastal transformation of swell [*Bromirski et al*., 2010], or result from other propagating long-period ocean waves transformed by topography at either the continental shelf break or the deeper continental shelf north of the RIS. The response of the ocean to a propagating storm system depends on the depth of the sea level pressure (SLP) low, the pressure gradient (winds), and the storm propagation speed, similar to storm surge along coastlines [*Bromirski et al*., 2017]. This mechanism in the deep ocean may generate the long period gravity waves that excite the RIS. Other possibilities include high-wave number coastally trapped mixed-vertical-mode Kelvin-like waves [*Kusahara et al*., 2014], eddies, and/or internal waves generated north of the RIS front.

Beamforming also shows relatively strong low-slowness extensional Lamb wave signals during the July 2015 event (Figures 7a and 7c), analogous to the extensional Lamb waves identified during the May IG event (Figure 4d). These results indicate that relatively strong flexural-gravity and extensional Lamb waves are excited throughout the year.

5. Comparison of Tsunami and Mid-Winter VLP Displacements

The spatial variability of the flexural-gravity wave seismic response across the RIS was characterized by the 95th percentile levels of ranked seismic displacement amplitudes during the tsunami 17–19 September 2015 and the mid-winter 5–11 July 2015 VLP events (Figure 8). The 95th percentile levels give conservative

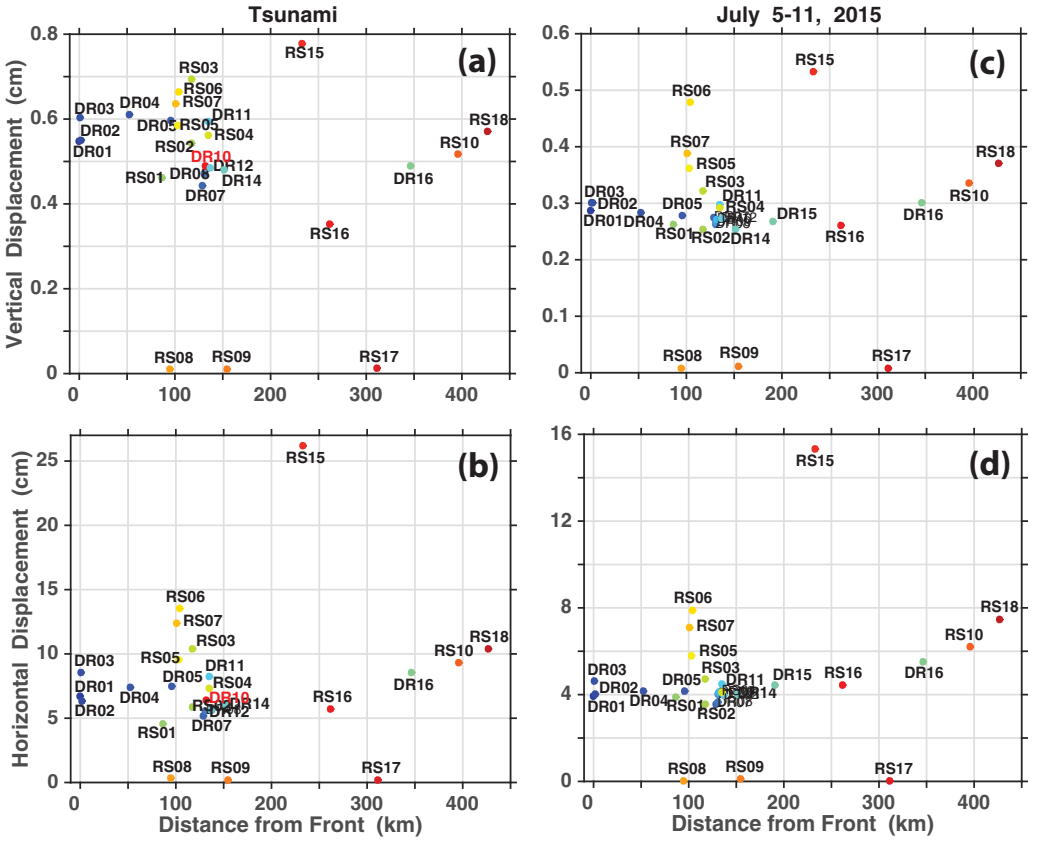

Figure 8. (a) Comparison of 95th percentile levels of observed RIS vertical and (b) horizontal displacements band pass-filtered over (0.001–0.01 Hz) during the 17–19 September tsunami excitation. (c and d) Same as (a) and (b) except for the austral winter 5–11 July event. 95th percentiles give conservative estimates of the peak RIS response. Note that displacement amplitude ranges (vertical axes) differ. Peak-to-trough amplitudes are about twice as large as those shown. RS08, RS09, and RS17 are on grounded ice. Different station colors are used only for identification purposes, and are the same in all plots.

estimates of the magnitude of peak vertical and horizontal displacements, excluding high amplitude transients resulting from local site effects, icequakes, and other episodic motions that are not due to flexural-gravity waves induced by gravity wave forcing.

Typically higher year-round observations (Figures 6a and 6b) indicate that horizontal displacements across the RIS are much larger than vertical by a factor of 10 or more. Tsunami-induced displacements are higher than those of the July VLP event, with the horizontal displacements about twice as large. Additionally, winter horizontal displacements in July (Figure 6b) are about twice those during the austral summer in January. These differences must result from differences in respective incident gravity wave amplitudes, although gravity wave incident angles likely are a factor. Somewhat larger horizontal displacements are observed east of the orthogonal transect stations (i.e., at RS05, RS06, RS07), and easternmost shelf front station DR03 levels are generally higher than farther west stations DR01 and DR02 (Figure 8b and 8d).

Substantially higher vertical and horizontal displacements are consistently observed at RS15 (Figure 8), positioned above or near a bathymetric high that constricts the thickness of the water layer (see supporting information Figure S6), which would tend to amplify the RIS flexural-gravity wave response [*Sergienko*, 2010]. Very low displacements are observed at stations on grounded ice at Roosevelt Island where the water layer is absent (RS08 and RS09) and at Steershead Ice Rise (RS17).

The tsunami, July VLP, and January swell/IG gravity wave events have different source regions resulting in different approach angles to the RIS front. However, the relative spatial displacement patterns for the three types of gravity wave forcing are similar (Figures 8 and supporting information Figure S5a). This similarity suggests that the pattern of the RIS response is more strongly controlled by bathymetry and changing dimensions of the ice shelf/water-layer system than by gravity wave source characteristics.

6. Large-Scale RIS Flow Velocity From Navigational GPS

Macroscale ice shelf motions have been previously well-characterized using multiple satellite interferometric synthetic-aperture radar data acquired during the International Polar Year 2007–2009 [*Rignot et al*., 2011a, 2011b]. However, intermittent observations cannot describe the spatial and temporal distribution of episodic motions, or whether ocean gravity wave forcing excites RIS responses that initiate fracturing sequences. High flow velocity regions are likely associated with episodic strains (particularly near rifts), potentially resulting from gravity wave-induced dynamic strains. Relatively short-term flow velocity estimates can be determined at the seismic stations from navigational GPS location data collected at each station.

Ice flow velocities at each seismic station were estimated from "hourly" state-of-health Iridium transmissions that included navigational GPS locations. While the individual GPS locations exhibit significant variability, averages of hourly estimates reduce the uncertainty in locations and associated ice flow estimates to useful ranges. Least squares navigational GPS ice flow velocity estimates over a 3 month period (black vectors in Figure 9a) compare well with MEaSUREs Earth Science Data Record (ESDR), National Snow and Ice Data Center (NSIDC) velocities (*Rignot et al*. [2011a, 2011b]; colored contours in Figure 9a). Velocities along the orthogonal transect from ice front station DR02 to RS18 (about 430 km south of the ice edge) show ice flow velocities that decrease with distance from the front (Figure 9b), consistent with *Rignot et al*. [2011a, 2011b] estimates. Navigational GPS-derived ice flow directions differ somewhat from flow directions inferred from the velocity contours, particularly near the RIS front, but are generally in close agreement with the MEaSUREs ice flow velocity estimates.

7. Tsunami Modeling

Modeled tsunami amplitudes across the RIS provide a "known" forcing with which to compare the observed Chilean tsunami-forced response with the year-long seismic array observations when tsunami forcing is absent. There are three components to the tsunami modeling: source function, bathymetry, and the actual propagation model. Clearly, uncertainty in the source function is problematic for matching tsunami observations in the far field, particularly on relatively small spatial scales in continental shelf (shallow) water. The tsunami source function is estimated from DART buoys, whose proximity to the earthquake rupture and number of proximal buoys is problematic. Furthermore, other gravity waves from other sources are arriving at the same time as the tsunami with energy in the swell, IG, and VLP bands. The RIS seismic data

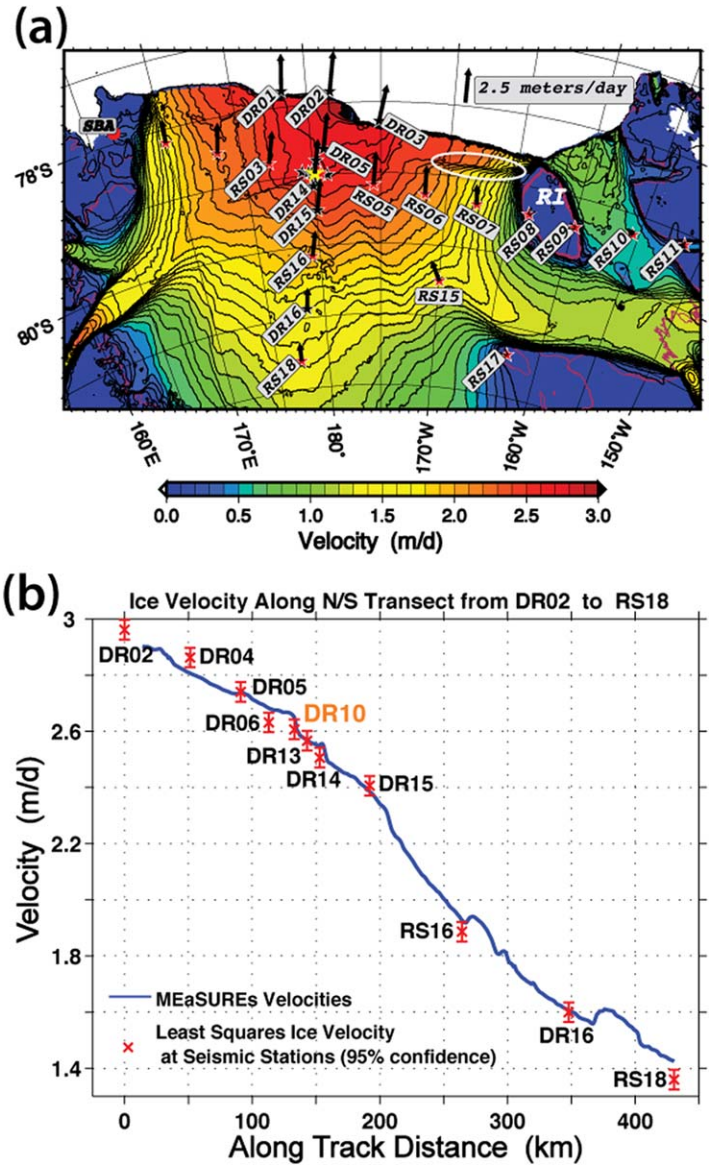

Figure 9. (a) Ice flow speeds and directions at the seismic stations determined from XEOS navigational GPS hourly state-of-health Iridium satellite transmissions during December 2014 to February 2015 (arrows: length proportional to the reference vector at the top) overlaid on contoured NSIDC *MEaSUREs* ice flow velocities [*Rignot et al.*, 2011a, 2011b]. Reference vector length (2.5 m d^{-1}, 0.9125 km a^{-1}) oriented north-south is shown at the top. A high flow-velocity-gradient region associated with rifting west of Roosevelt Island (*RI*) is indicated by the white ellipse. (b) Comparison between XEOS (red x's with error bars) and *MEaSUREs* (blue line) ice flow velocity estimates. DR10 location is indicated by the yellow star in Figure 9a (see also Figure 1).

comparisons here are not intended to validate tsunami model results, but to compare peak amplitude spatial variability. Observed peak RIS seismic amplitudes for the Chilean tsunami occur in consort with modeled peak tsunami amplitudes, allowing investigation of the effect of gravity wave directionality and Ross Sea embayment bathymetry on tsunami amplitudes along the RIS front as well as beneath the ice shelf to the grounding zone. Additionally, the similarity in spectral levels of the RIS response to tsunami and VLP gravity wave forcing (Figures 3 and 6c, 6d, respectively) and their respective displacement patterns (Figure 8) indicates that tsunami model data within the Ross Sea embayment can inform on non-tsunami VLP gravity wave-forced variability.

The Chilean tsunami was modeled using the Method of Splitting Tsunamis (MOST) numerical code [*Titov and González*, 1997]. MOST solves the nonlinear shallow-water wave equation in polar coordinates. The MOST code was used in combination with the IBCSO [*Arndt et al.*, 2013] bathymetric data set to model tsunami amplitudes in the Ross Sea embayment. The tsunami source function at the earthquake rupture region was inverted from near-source DART data [*Meinig et al.*, 2005; *Tang et al.*, 2016], and produces reasonably good agreement with DART observations throughout the Pacific Ocean. The tsunami simulation proceeded in two stages. First, wave activity in deep water was modeled as it propagated from the tsunami source area to just north of the RIS at latitude 60°S using a 4 arc min grid. Second, to capture higher-frequency waves likely to develop due to tsunami interaction with the local the Ross Sea bathymetry, shallow-water tsunami evolution across the Antarctic continental slope and the Ross Sea north of the RIS region was propagated across the Ross Sea embayment to the grounding line. The model employed a resolution of 2 arc min along lines of longitude and 1 arc min along lines of latitude. Tsunami simulations did not include the ice shelf.

The modeled Chilean tsunami arrives dominantly from the east (see supporting information Animation S1), with deep water wave fronts traveling roughly orthogonal to the shelf front. This approach direction

necessarily directs much of the tsunami energy toward the western boundary of the Ross Sea embayment. The ice shelf is much thinner than the wavelengths of tsunami and VLP waves, so the tsunami propagation to the RIS grounding zone will not be greatly affected by the ice covering. The tsunami-induced flexural-gravity wave response, represented by spectral levels in the VLP band in Figures 3 and 6, do not attenuate, confirms that the ice covering has minimal effect, if any, on this part of the gravity wave spectrum.

The tsunami forcing at the RIS front varies spatially and temporally. To characterize the seismic response across the RIS, ranked 95th-percentile vertical seismic displacements during the Chilean tsunami were determined. The nonice-covered Ross Sea embayment tsunami model amplitudes vary within a relatively

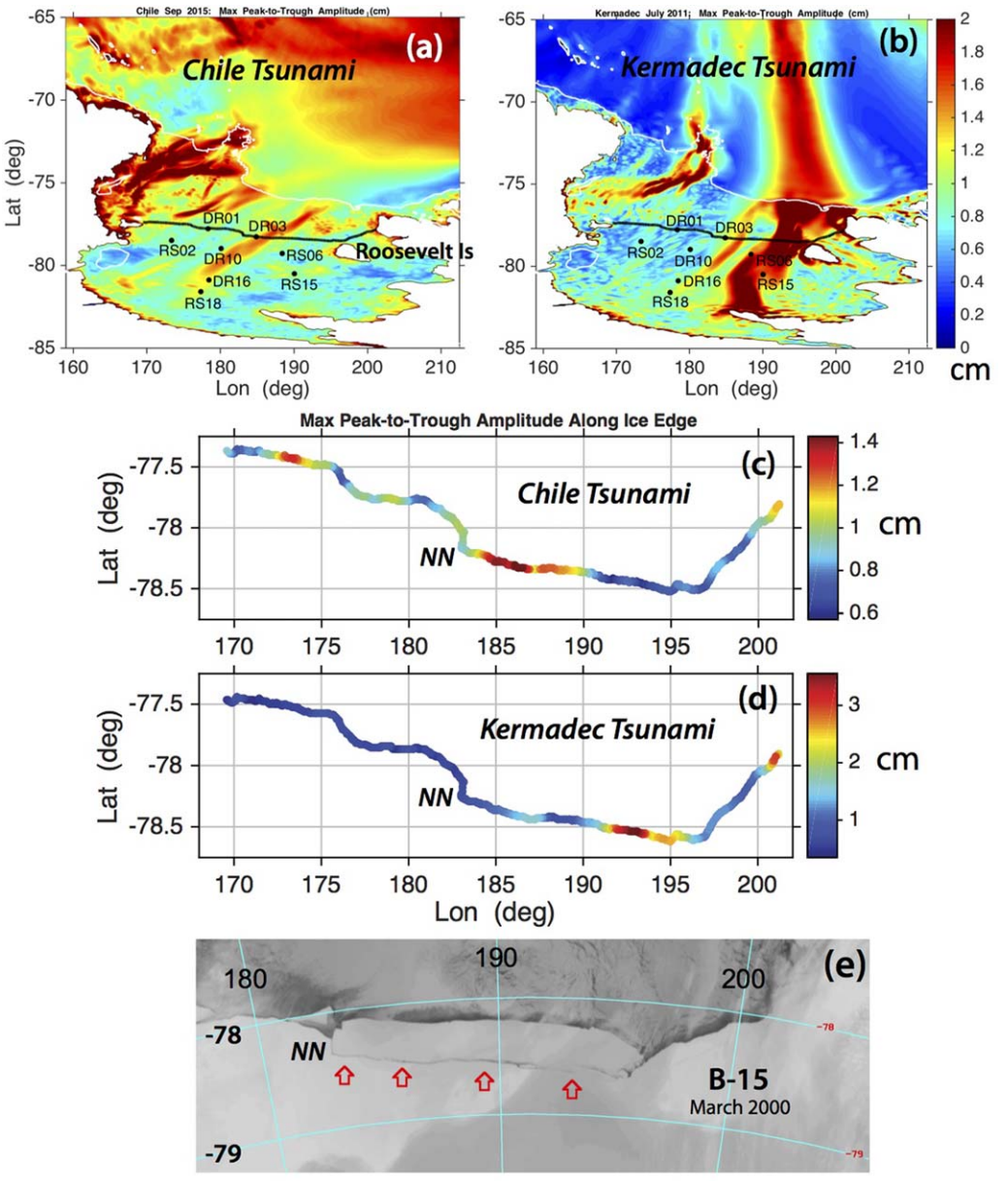

Figure 10. Modeled tsunami amplitudes at the Ross Ice Shelf. (a) Regional maps of the maximum peak-to-trough tsunami amplitudes for: (a) 16 September 2015 Chilean tsunami arriving from the east (earthquake epicenter 31.570°S, 71.654°W), with locations of Roosevelt Island and several seismic stations shown, and (b) the 6 July 2011 Kermadec tsunami (29.312°S, 176.204°W) arriving from the north (amplitude scale applies to both). The ice front (thick black line) and the 1000 m isobath (thin white line) representing the continental slope break are indicated. (c and d) Maximum peak-to-trough modeled tsunami amplitudes along the ice edge for the Chilean and Kermadec tsunamis, respectively. The Nascent notch (NN) at the western edge of tabular iceberg B-15 is indicated. (e) Satellite image of B-15 (red arrows) during March 2000 near the time of calving (courtesy of Antarctic Meteorology Research Center, University of Wisconsin, Madison). Associated animations of these tsunami events can be found in the supporting information.

narrow range (about 0.10 cm; supporting information Figure S5b), in contrast to an about 0.5 cm range of observed on-ice vertical displacement amplitudes (Figure 8a). This difference may result from underestimated tsunami amplitudes and/or effects of the gravity wave/ice shelf interactions.

The tsunami and other VLP gravity wave approach angles can have a significant effect on the amplitude distribution across the Ross Sea embayment. The bathymetric effect on ocean gravity wave amplitudes across the RIS front is illustrated by comparison of the modeled 6 July 2011 Kermadec tsunami (Figure 10b) and modeled Chilean tsunami (Figure 10a). In contrast to the westward-propagating Chilean tsunami, the Kermadec tsunami propagated from the north (source location 29.312°S, 176.204°W), yielding wave fronts that were nearly parallel to the shelf front (see supporting information Animation S2).

The Kermadec tsunami produces a significantly different wave amplitude distribution across the RIS than that of the Chilean tsunami. Of note is the significant effect of Roosevelt Island (RI in Figures 9a and 10b) on Kermadec tsunami amplitudes near the RIS front eastern boundary (see supporting information Animation S2), resulting in energy reflection and refraction that amplifies wave heights west of Roosevelt Island. Similar VLP gravity wave forcing may be instrumental in rift development near islands [*Braun et al*., 2009], which is exemplified at the RIS by the differential ice flow velocities west of Roosevelt Island (within the white oval in Figure 9a that identifies the rift location).

The influence of bathymetry is further demonstrated by the modeled Chilean and Kemadec tsunamis maximum peak-to-trough amplitudes shown in Figures 10a and 10b, respectively. Although gravity waves impact the entire RIS front, certain regions along the front are preferentially more strongly excited. Features common to both tsunamis reflect bathymetric controls that concentrate incident gravity wave energy along certain portions of the RIS front, particularly the region along the front east of the Nascent notch (NN in Figures 10c–10e) that delineates the western boundary of tabular iceberg B-15. Their common frequency band indicates that the bathymetric effect on tsunami and VLP gravity waves must be similar, resulting in continuous enhanced forcing west of Roosevelt Island. This suggests that the bathymetric focusing of persistent IG and VLP wave impacts and the location of B-15 calving (Figure 10e) are not coincidental.

8. Discussion

The persistent high vertical and horizontal displacements (Figures 6a and 6b) and high beam power at low frequencies ($<$0.01 Hz) near 15 s/km (Figures 4a, 4b, and 7a) indicate that flexural-gravity wave excitation occurs nearly continuously throughout the year. Continuous oscillatory strain across the RIS has the potential for fatigue weakening of the ice and expansion of existing fractures. In addition, because of the lack of discernable attenuation, it seems likely that VLP ($>$300 s period) flexural-gravity wave energy reaches the grounding line. The propagation of vertical and horizontal displacements across the ice shelf/ice-sheet transition (grounding) zone could transmit stresses from the ice shelf into the ice sheet that may play a role in grounding zone dynamics [*Schoof*, 2007].

The importance of bathymetric controls north of the ice edge and below the ice are demonstrated by the distribution of maximum tsunami model amplitudes along the RIS front (Figures 8a,b), and the anomalously high displacements at RS15, which lies above a bathymetric high that reduces the water column thickness to $\sim$100 m [BEDMAP2; *Fretwell et al*., 2013] (Figure 8). Thus, we speculate that it is likely not a coincidence that the region of the RIS front that experiences enhanced bathymetrically focused gravity wave forcing coincides with the B-15 (Figure 10e) and C-16 [*MacAyeal et al*., 2009] tabular iceberg calving locations, although stresses resulting from the RIS grounding at Roosevelt Island could also be a factor that contributes to rift formation in that region, similar to island effects at the Wilkins Ice Shelf [*Braun et al*., 2009]. Because tsunami and nontsunami VLP events produce similar flexural-gravity wave responses, nearly continuous high amplitude austral winter flexural-gravity wave-induced vertical and horizontal displacements provide forcing that likely contributes to tabular iceberg calving and rift propagation, potentially triggering these fracture events. The ubiquitous nature of gravity wave activity necessarily indicates that all ice shelves are subject to similar persistent forcing that can affect long-term ice shelf evolution.

While the dynamical gravity wave-induced seismic displacements are relatively large, it is unclear whether measureable static strains result. However, extensional dynamical strains estimated for a propagating 0.002 Hz (500 s period) flexural-gravity wave traveling at 70 m/s are about 5×10^{-6} and 7×10^{-7} for 20 cm

horizontal and 0.25 cm vertical cyclic amplitudes, respectively [*Aki and Richards*, 1980], potentially facilitating crack expansion and/or fatigue failure in the ice [*Holdsworth and Glynn* 1978]. To investigate whether ice shelf/ocean-gravity wave interactions result in static episodic strains on the RIS, a 13-station geodetic array was deployed during November 2015. The geodetic GPS stations were colocated with shelf front and orthogonal transect seismic stations from DR02 to RS18. GPS data collected from November 2015 to November 2016 were recovered during the 2016 field season. GPS-measured episodic strains associated with synoptic gravity wave arrivals (identified with the seismic array data) will further establish the relationship between gravity wave impacts and ice shelf mechanical responses.

Gravity wave-induced displacements at other narrower West Antarctic ice shelf grounding zones are potentially larger than those observed at the RIS. This is because significant IG band energy (Figure 3), in addition to VLP motions, can reach Amundsen Sea grounding zones (e.g., the Getz Ice Shelf grounding zone is about 100 km from the shelf front). In addition, the closer approach of the Antarctic Circumpolar Current (ACC) to the Amundsen Sea coast potentially results in more storm-forced gravity wave energy being directed at Amundsen Sea ice shelves. An intensification and poleward shift of the southern annular mode (SAM) would cause a southward displacement of the ACC [*Boening et al*., 2008; *Hemer et al*., 2010], directing more gravity wave energy southward in addition to facilitating transport of warm ocean water to West Antarctic ice shelves [*Gille*, 2014]. Thus, the gravity wave-induced displacements and resulting impacts at more northern West Antarctic ice shelf grounding zones are potentially larger than at the RIS. Higher gravity wave amplitudes anticipated in the coming decades under projected increases in Southern Ocean storm intensity would increase associated impacts on West Antarctic ice shelves.

9. Conclusions

The first broadband seismographic recordings of tsunami-induced ice shelf displacements were used to characterize the spatial variability of the response of an ice shelf to gravity wave impacts. Gravity waves spanning infragravity (IG) wave to tsunami frequencies (0.02–0.001 Hz) excite flexural-gravity waves that vibrate the RIS nearly continuously throughout the year, with the highest amplitudes in this frequency band observed during the austral winter. The induced flexural-gravity waves propagate from the front to the deep interior of the ice shelf at gravity wave speeds, about 70 m/s. RIS displacements, excited by tsunami and other very long period (VLP) gravity waves, are dominated by flexural-gravity waves at periods $>$300 s (i.e., $<$0.003 Hz) that propagate nearly unattenuated across the RIS, reaching the grounding zone. In contrast, flexural-gravity waves in the shorter period IG band (0.003–0.02 Hz) attenuate with distance from the shelf front, resulting in VLP energy dominating at locations more than 100 km or so from the shelf front. Bathymetry both north and south of the shelf front concentrates gravity wave energy at particular RIS front locations, possibly influencing rift development and tabular iceberg calving west of Roosevelt Island. Water layer thickness has a significant effect of flexural-gravity wave displacement amplitudes, with substantially higher amplitude responses at seismic stations where seafloor bathymetry constricts the thickness of the water layer.

Acknowledgments
Bromirski, Gerstoft, Chen, and Diez were supported by NSF grant PLR 1246151. Stephen was supported by NSF grant PLR-1246416. Wiens, Aster, and Nyblade were supported under NSF grants PLR-1142518, 1141916, and 1142126, respectively. Arcas was supported by the National Oceanic and Atmospheric Administration (NOAA), with this report being PMEL contribution 4648. Seismic instruments and on-ice installation support were provided by the Incorporated Research Institutions for Seismology (IRIS) through the PASSCAL Instrument Center at New Mexico Tech. The RIS seismic data are archived at the IRIS Data Management Center, http://ds.iris.edu/ds/nodes/dmc/. Tsunami model outputs are archived at the NOAA National Center for Environmental Information, https://data.noaa.gov/dataset. The facilities of the IRIS Consortium are supported by the National Science Foundation under Cooperative Agreement EAR-1261681 and the DOE National Nuclear Security Administration. O. Sergienko provided helpful discussions and comments. We thank Patrick Shore, Michael Baker, Cai Chen, Robert Anthony, Reinhard Flick, Jerry Wanetick, Weisen Shen, and Tsitsi Madziwa Nussinov for their help with field operations, and Tom Bolmer for map construction. Logistical support from the U.S. Antarctica Program in McMurdo is much appreciated.

References

Aki, K., and P. G. Richards (1980), *Quantitative Seismology, Theory and Methods*, vol. 1, 557 pp., Freeman-Price, San Francisco, Calif.

Anthony, R., R. Aster, and D. McGrath (2017), Links between atmosphere, ocean, and cryosphere from two decades of microseism observations on the Antarctic Peninsula, *J. Geophys. Res. Earth Surf.*, *122*, 153–166, doi:10.1002/2016JF004098.

Aránguiz, R., et al. (2016), The 16 September 2015 Chile tsunami from the post-tsunami survey and numerical modeling perspectives, *Pure Appl. Geophys.*, *173*, 333–348, doi:10.1007/s00024-015-1225-4.

Arndt, J. E., et al. (2013), The international bathymetric chart of the Southern Ocean (IBCSO) Version 1.0—A new bathymetric compilation covering circum-Antarctic waters, *Geophys. Res. Lett.*, *40*, 3111–3117, doi:10.1002/grl.50413.

Banwell, A. F., D. R. MacAyeal, and O. V. Sergienko (2013), Break-up of the Larsen B Ice Shelf triggered by chain-reaction drainage of supraglacial lakes, *Geophys. Res. Lett.*, *40*, 5872–5876, doi:10.1002/2013GL057694.

Beyreuther, M., R. Barsch, L. Krischer, T. Megies, Y. Behr, and J. Wassermann (2010), ObsPy: A Python toolbox for seismology, *Seismol. Res. Lett.*, *81*(3), 530–533.

Boening, C. W., A. Dispert, M. Visbeck, S. R. Rintoul, and F. U. Schwarzkopf (2008), The response of the Antarctic Circumpolar Current to recent climate change, *Nat. Geosci.*, *1*, 864–869. [Available at http://www.nature.com/ngeo/journal/v1/n12/suppinfo/ngeo362_S1.html.]

Braun, M., A. Humbert, and A. Moll (2009), Changes of Wilkins Ice Shelf over the past 15 years and inferences on its stability, *The Cryosphere*, *3*, 41–46.

Bromirski, P. D., and R. A. Stephen (2012), Response of the Ross Ice Shelf, Antarctica, to ocean gravity-wave forcing, *Ann. Glaciol.*, *53*(60), 163–172, doi:10.3189/2012AoG60A058.

Bromirski, P. D., O. V. Sergienko, and D. R. MacAyeal (2010), Transoceanic infragravity waves impacting Antarctic ice shelves, *Geophys. Res. Lett.*, *37*, L02502, doi:10.1029/2009GL041488.
Bromirski, P. D., A. Diez, P. Gerstoft, R. A. Stephen, T. Bolmer, D. A. Wiens, R. C. Aster, and A. Nyblade (2015), Ross ice shelf vibrations, *Geophys. Res. Lett.*, *42*, 7589–7597, doi:10.1002/2015GL065284.
Bromirski, P. D., R. E. Flick, and A. J. Miller (2017), Storm surge along the Pacific coast of North America, *J. Geophys. Res. Oceans*, *121*, 441–457, doi:10.1002/2016JC012178.
Bromwich, D. H., and J. P. Nicolas (2010), Sea-level rise: Ice-sheet incertainty, *Nat. Geosci.*, *3*, 596–597, doi:10.1038/ngeo946.
Brunt, K. M., E. Okal, and D. R. MacAyeal (2011), Antarctic ice-shelf calving triggered by the Honshu (Japan) earthquake and tsunami, March 2011, *J. Glaciol.*, *57*(205), 785–788.
Cathles, L. M., IV, E. A. Okal, and D. R. MacAyeal (2009), Seismic observations of sea swell on the floating Ross Ice Shelf, Antarctica, *J. Geophys. Res.*, *114*, F02015, doi:10.1029/2007JF000934.
Crocker, G. B., and P. Wadhams (1988), Observations of wind generated waves in Antarctic fast ice, *J. Phys. Oceangr.*, *18*(9), 1291–1299.
Diez, A., P. D. Bromirski, P. Gerstoft, R. A. Stephen, T. Bolmer, D. A. Wiens, R. C. Aster, and A. Nyblade (2016), Ice shelf structure derived from dispersion curve analysis of ambient seismic noise, Ross Ice Shelf, Antarctica, *Geophys. J. Int.*, *205*, 785–795, doi:10.1093/gji/ggw036.
Dupont, T. K., and R. B. Alley (2005), Assessment of the importance of ice-shelf buttressing to ice-sheet flow, *Geophys. Res. Lett.*, *32*, L04503, doi:10.1029/2004GL022024.
Fox, C., and V. A. Squire (1991), Coupling between the ocean and an ice shelf, *Ann. Glaciol.*, *15*, 101–108.
Fretwell, P., et al. (2013), Bedmap2: Improved ice bed, surface and thickness datasets for Antarctica, *The Cryosphere*, *7*, 375–393, doi:10.5194/tc-7-375-2013.
Gerstoft, P., and T. Tanimoto (2007), A year of microseisms in southern California, *Geophys. Res. Lett.*, *34*, L20304, doi:10.1029/2007GL031091.
Gille, S. (2014), How ice shelves melt, *Science*, *346*, 1180–1181, doi:10.1126/science.aaa0886.
Graff, K. (1975), *Wave Motion in Elastic Solids*, 649 pp., Dover, New York.
Gudmundsson, G. H. (2013), Ice-shelf buttressing and the stability of marine ice sheets, *The Cryosphere*, *7*, 647–655, doi:10.5194/tc-7-647-2013.
Harmon, N., C. Rychert, and P. Gerstoft (2010), Distribution of noise sources for seismic interferometry, *Geophys. J. Int.*, *183*, 1470–1484, doi:10.1111/j.1365-246X.2010.04802.
Hemer, M. A., J. A. Church, and J. R. Hunter (2010), Variability and trends in the directional wave climate of the Southern Hemisphere, *Int. J. Climatol.*, *30*, 475–491, doi:10.1002/joc.1900.
Herbers, T. H. C., S. Elgar, and R. T. Guza (1995), Generation and propagation of infragravity waves, *J. Geophys. Res.*, *100*(C12), 24,863–24,872.
Holdsworth, G., and J. Glynn (1978), Iceberg calving from floating glaciers by a vibrating mechanism, *Nature*, *274*, 464–466.
Joughin, I., and R. B. Alley (2011), Stability of the West Antarctic ice sheet in a warming world, *Nat. Geosci.*, *4*, 506–513, doi:10.1038/ngeo1194.
Kusahara, K., and K. I. Ohshima (2014), Kelvin waves around Antarctica, *J. Phys. Oceangr.*, *44*, 2909–2920, doi:10.1175/JPO-D-14-0051.1.
Lamb, H. (1917), On waves in an elastic plate, *Proc. R. Soc. London, Ser. A*, *93*(648), 114–128.
MacAyeal, D. R., et al. (2006), Transoceanic wave propagation links iceberg calving margins of Antarctica with storms in tropics and Northern Hemisphere, *Geophys. Res. Lett.*, *33*, L17502, doi:10.1029/2006GL027235.
MacAyeal, D. R., E. A. Okal, R. C. Aster, and J. N. Bassis (2009), Seismic observations of glaciogenic ocean waves (micro-tsunamis) on icebergs and ice shelves, *J. Glaciol.*, *55*(190), 193–206.
MacAyeal, D. R., O. V. Sergienko, and A. F. Banwell (2015), A model of viscoelastic ice-shelf flexure, *J. Glaciol.*, *61*(228), 635–645, doi:10.3189/2015JoG14J169.
Meinig, C., S. E. Stalin, A. I. Nakamura, and H. B. Milburn (2005), *Real-Time Deep-Ocean Tsunami Measuring, Monitoring, and Reporting System: The NOAA DART II Description and Disclosure*, 15 pp., NOAA/Pac. Mar. Environ. Lab., Seattle, Wash. [Available at http://nctr.pmel.noaa.gov/Dart/Pdf/DART_II_Description_6_4_05.pdf.]
Press, F., and M. Ewing (1951), Propagation of elastic waves in a floating ice sheet, *Trans. AGU*, *32*(5), 673–678.
Rack, W., and H. Rott (2004), Pattern of retreat and disintegration of Larsen B ice shelf, Antarctic Peninsula, *Ann. Glaciol.*, *39*, 505–510, doi:10.3189/172756404781841405.
Rasmussen, L., P. D. Bromirski, A. J. Miller, D. Arcas, R. E. Flick, and M. C. Henderschott (2015), Source location impact on relative tsunami strength along the U.S. West Coast, *J. Geophys. Res. Oceans*, *120*, 4945–4961, doi:10.1002/2015JC010718.
Rignot, E., G. Casassa, P. Gogineni, W. Krabill, A. Rivera, and R. Thomas (2004), Accelerated ice discharge from the Antarctic Peninsula following collapse of Larsen B ice shelf, *Geophys. Res. Lett.*, *31*, L18401, doi:10.1029/2004GL020679.
Rignot, E., J. Mouginot, and B. Scheuchl (2011a), Ice flow of the Antarctic ice sheet, *Science*, *333*(6048), 1427–1430, doi:10.1126/science.1208336.
Rignot, E., J. Mouginot, and B. Scheuchl (2011b), *MEaSUREs InSAR-Based Antarctica Ice Velocity Map*, NASA DAAC at the Natl. Snow and Ice Data Cent., Boulder, Colo., doi:10.5067/MEASURES/CRYOSPHERE/nsidc-0484.001.
Scambos, T. A., J. A. Bohlander, C. A. Shuman, and P. Skvarca (2004), Glacier acceleration and thinning after ice shelf collapse in the Larsen B embayment, Antarctica, *Geophys. Res. Lett.*, *31*, L18402, doi:10.1029/2004GL020670.
Scambos, T., H. A. Fricker, C.-C. Liu, J. Bohlander, J. Fastook, A. Sargent, R. Massom, and A.-M. Wu (2009), Ice shelf disintegration by plate bending and hydro-fracture: Satellite observations and model results of the 2008 Wilkins ice shelf break-ups, *Earth Planet. Sci. Lett.*, *280*(1–4), 51–60.
Schoof, C. (2007), Ice sheet grounding line dynamics: Steady states, stability, and hysteresis, *J. Geophys. Res.*, *112*, F03S28, doi:10.1029/2006JF000664.
Sergienko, O. V. (2010), Elastic response of floating glacier ice to impact of long-period ocean waves, *J. Geophys. Res.*, *115*, F04028, doi:10.1029/2010JF001721.
Sergienko, O. V. (2013), Normal modes of a coupled ice-shelf/sub-ice-shelf cavity system, *J. Glaciol.*, *59*(213), 76–80, doi:10.3189/2013JoG12J096.
Squire, V. (2007), Of ocean waves and sea-ice revisited, *Cold Reg. Sci. Technol.*, *49*(2), 110–133.
Tang, L., V. V. Titov, C. Moore, and Y. Wei (2016), Real-time assessment of the 16 September 2015 Chile tsunami and implications for near-field forecast, *Pure Appl. Geophys.*, *173*(2), 369–387, doi:10.1007/s00024-015-1226-3.
Titov, V., and F. I. González (1997), Implementation and testing of the Method of Splitting Tsunami (MOST) model, *NOAA Tech. Memo, ERL PMEL-112 (*PB98–122773*)*, 11 pp., NOAA/Pac. Mar. Environ. Lab., Seattle, Wash.
Traer, J., and P. Gerstoft (2013), A unified theory of microseisms and hum, *J Geophys. Res.*, *119*, 3317–3339, doi:10.1002/2013JB010504.
Uchiyama, Y., and J. C. McWilliams (2008), Infragravity waves in the deep ocean: Generation, propagation, and seismic hum excitation, *J. Geophys. Res.*, *113*, C07029, doi:10.1029/2007JC004562.
Wadhams, P., and M. J. Doble (2009), Sea ice thickness measurement using episodic infragravity waves from distant storms, *Cold Reg. Sci. Technol.*, *56*, 98–101, doi:10.1016/j.coldregions.2008.12.002.
Williams, R. T., and E. S. Robinson (1981), Flexural waves in the Ross Ice Shelf, *J. Geophys. Res.*, *86*(C7), 6643–6648.